Research Article

Real-Time Monitoring of Morphology and Optical Properties during Sputter Deposition for Tailoring Metal–Polymer Interfaces

Matthias Schwartzkopf,*,[†] Gonzalo Santoro,[†,‖] Calvin J. Brett,[†] André Rothkirch,[†] Oleksandr Polonskyi,[‡] Alexander Hinz,[‡] Ezzeldin Metwalli,[§] Yuan Yao,[§] Thomas Strunskus,[‡] Franz Faupel,[‡] Peter Müller-Buschbaum,[§] and Stephan V. Roth[†]

[†]Photon Science, Deutsches Elektronen-Synchrotron (DESY), Notkestr. 85, D-22607 Hamburg, Germany

[‡]Lehrstuhl für Materialverbunde, Institut für Materialwissenschaft, Christian Albrechts-Universität zu Kiel, Kaiserstr.2, D-24143 Kiel, Germany

[§]Lehrstuhl für Funktionelle Materialien, Physik-Department, Technische Universität München, James-Franck-Str. 1, D-85748 Garching, Germany

S *Supporting Information*

ABSTRACT: The reproducible low-cost fabrication of functional metal–polymer nanocomposites with tailored optoelectronic properties for advanced applications remains a major challenge in applied nanotechnology. To obtain full control over the nanostructural evolution at the metal–polymer interface and its impact on optoelectronic properties, we employed combined in situ time-resolved microfocus grazing incidence small angle X-ray scattering (μGISAXS) with in situ UV/vis specular reflectance spectroscopy (SRS) during sputter deposition of gold on thin polystyrene films. On the basis of the temporal evolution of the key scattering features in the real-time μGISAXS experiment, we directly observed four different growth regimes: nucleation, isolated island growth, growth of larger aggregates via partial coalescence, and continuous layer growth. Moreover, their individual thresholds were identified with subnanometer resolution and correlated to the changes in optical properties. During sputter deposition, a change in optical reflectivity of the pristine gray-blue PS film was observed ranging from dark blue color due to the presence of isolated nanoclusters at the interface to bright red color from larger Au aggregates. We used simplified geometrical assumptions to model the evolution of average real space parameters (distance, size, density, contact angle) in excellent agreement with the qualitative observation of key scattering features. A decrease of contact angles was observed during the island-to-percolation transition and confirmed by simulations. Furthermore, a surface diffusion coefficient according to the kinetic freezing model and interfacial energy of Au on PS at room temperature were calculated based on a real-time experiment. The morphological characterization is complemented by X-ray reflectivity, optical, and electron microscopy. Our study permits a better understanding of the growth kinetics of gold clusters and their self-organization into complex nanostructures on polymer substrates. It opens up the opportunity to improve nanofabrication and tailoring of metal–polymer nanostructures for optoelectronic applications, organic photovoltaics, and plasmonic-enhanced technologies.

KEYWORDS: metal–polymer nanocomposites, gold cluster growth kinetics, sputter deposition, in situ GISAXS, UV/vis specular reflectance spectroscopy
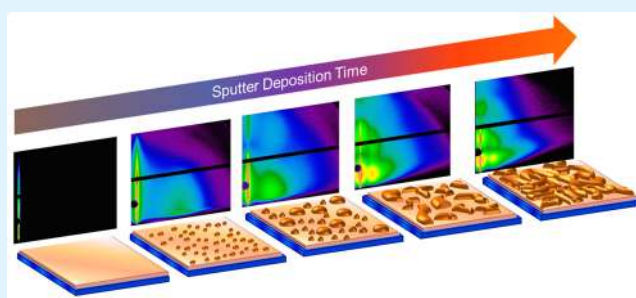
INTRODUCTION

Since the dawn of nanotechnology, one of the primary objectives has been to obtain a fully controlled process to fabricate nanostructures on a larger scale with tailored properties using self-organizing principles.[1,2] Hereby, gold as a noble metal with remarkable relativistic quantum chemistry[3] combined with excellent chemical stability presents various promising advanced applications in form of supported nanoclusters, for example, in heterogeneous catalysis and optoelectronics.[4,5] The final device performance, in particular for optoelectronics, strongly depends on cluster size distribution, shape, surface chemistry, and arrangement.[6,7] In catalysis,

the perimeter of a gold cluster creates catalytic-active binding sites at the interface, for example, enabling the oxidative conversion of toxic CO into CO_2 even at a temperature of 40 K.[8,9] Moreover, an increase in light harvesting ability has been reported by introducing noble metal cluster layers in photovoltaics.[5,10−12]

In order to gain full control over the fabrication process and to obtain the desired final properties, in situ and real-time

investigation of growth kinetics during nanostructure evolution is crucial for advanced material research. In this field, metal–polymer nanocomposites stand out as attractive materials, mainly due to the versatility in combining the unique optoelectronic and magnetic properties of metallic nanostructures and the large variety of available polymer materials with adjustable physicochemical properties.[13] Furthermore, these nanocomposites present promising applications as flexible and inexpensive organic photovoltaics (OPV),[12,14] organic field effect transistors[15,16] (OFET), or organic light-emitting diodes (OLED).[17,18] Nevertheless, to fully exploit nanofabrication capabilities for optoelectronic applications it is essential to gain a deep understanding of the growth mechanisms and to correlate the nanostructures with their optical properties.

Initial description of the complex surface processes during the early stages of thin film growth can be traced back to the research activities of Venables and Lagally and their co-workers.[19,20] In this framework, grazing incidence small angle X-ray scattering (GISAXS) was introduced as a nondestructive and versatile surface sensitive technique to quantify post-deposition growth kinetics of supported gold clusters.[21] Later, the advanced application of microfocused synchrotron radiation established GISAXS to be a powerful in situ technique for morphological characterizations of thin films during fabrication processes such as vapor deposition[22−27] or evaporation-mediated self-assembly.[28−30] Due to the shallow incidence angle applied, GISAXS is a highly surface sensitive technique providing statistically relevant information on particles' shape and interparticle correlation distances over a macroscopic sample area. Especially the combination of GISAXS with sputter deposition proved to be a very powerful tool for the in situ growth characterization of thin nanostructured metallic films on inorganic substrates[24,25,31−33] and on a variety of organic templates,[22,23,26,34−36] even with subnanometer and millisecond resolution.[24−26]

Despite the fact that nowadays chemical synthesis allows precise control of size and shape of individual nanoparticles,[37] it is challenging to deposit individual nanoparticles on surfaces with high coverage using chemical techniques or to fabricate ramified nanostructures on surfaces with precise control of the surface coverage.[13] Especially, ramified structures have very interesting applications in plasmonics and sensors.[25,38] Another decisive advantage of physical methods like sputter deposition is the easily reproducible, low-cost, solvent-, reducing agent- and surfactant-free fabrication of such supported nanoclusters layers with tailored collective properties without any further chemical cleaning or processing. This holds especially for metal–polymer nanocomposites, where polymer thin films can change their morphology in the presence of solvents. In the case of functional metal–polymer nanocomposites prepared by sputter deposition, polymer-mediated self-assembly of metal clusters on polystyrene (PS) containing diblock copolymer films[39] and PS colloids has been investigated using in situ GISAXS. During sputter deposition of Co, Metwalli et al. showed that a selectively decoration of PS domains occurs on microphase-separated diblock copolymer films.[34] Schlage et al. followed the evolution of the magnetic state during Fe sputter deposition onto a highly ordered, nanoporous PS containing diblock copolymer resulting in a magnetic antidot array.[35] In the case of sputter deposition of Au on similar diblock copolymer thin films, a preferential accumulation of Au at PS domains occurs.[22] This selective wetting behavior is primarily attributed to the differences in surface mobility and interaction

of the Au adatoms with the PS domains.[39,40] In a recent study, the selectivity of Au on PS domains was exploited to fabricate directional hierarchically nanostructures with optical anisotropy via glancing angle sputter deposition.[41] Hence, exploring the metal–polymer interaction during self-organization of Au on PS homopolymer under controllable and reproducible conditions like sputter deposition forms a 2-fold scientific platform. On one hand, this model system serves to investigate practical preparation conditions and functional applications of metal–polymer nanocomposites.[13,28,38] On the other hand, it contributes to tackle fundamental scientific questions such as metal subsurface diffusion and its impact on the polymer thin films stability.[40,42,43]

In the present work, we investigate the basic principles of metal–polymer nanocomposite preparation via sputter deposition of Au on PS homopolymer thin films as a metal-dielectric/insulator model system. We have followed in situ and in real-time the morphological evolution of the nanostructured Au film and the related optical properties in the UV/vis regime during radio frequency (RF) sputter deposition by combining microfocus GISAXS (μGISAXS) together with UV/vis specular reflectance spectroscopy (SRS) measurements; the latter being a very sensitive method to study changes in the optical properties of thin films.[44,45] The combination of low deposition rates during RF sputter deposition with the high time resolution achieved during continuous metal layer deposition allows for observing early metal growth stages and extracting important morphological parameters as well as the thresholds involved in the nanostructure growth kinetics with subnanometer resolution.[25,26,41,46] All this information is significant for tuning the nanostructures for a large variety of organic optoelectronics such as OPVs and OLEDs, which is in turn beneficial for their low-cost fabrication, device performance, and optimized use of noble metals in general.

RESULTS AND DISCUSSION

To give an overview of the growth process, Figure 1 presents selected two-dimensional (2D) μGISAXS patterns obtained during sputter deposition of Au on PS thin film (for more details, see Supporting Information). After starting the sputter deposition process, a broad side peak ($q_{y,1,\max}$) emerges at large q_y values, indicating the presence of a laterally less ordered nanostructure arrangement on the polymer. As the deposition proceeds, the side peak becomes narrower and shifts toward smaller q_y values, whereas the peak shift significantly decelerates at later sputtering times. This observation is related to the lateral growth of nanostructures with increasing order until the cluster arrangement becomes constrained due to spatial restrictions. Moreover, additional peaks along q_z appear and shift toward lower q_z values during sputter deposition, indicating a vertical growth of the nanostructured thin film. The intensity distribution along q_z shows the typical thickness modulation similar to Kiessig fringes above the critical angle (Figure S4, Supporting Information). This scattering feature results from the refraction of the incident wave and subsequent reflection while matching the diffraction condition and thus guiding the wave through the thin film.[47] In addition, a shift of the intensity from the PS Yoneda peak to the critical angle of Au is visible, which is related to the increase of electron density. At an effective thickness of $\delta = 2.14 \pm 0.04$ nm, initially a broadening of the Yoneda region becomes clear resulting in a second side peak ($q_{y,2,\max}$) after 4.21 ± 0.09 nm continuous deposition (Figure S4, Supporting Information). This addi-
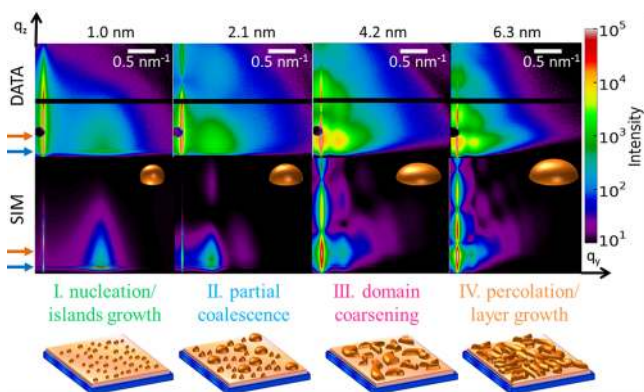
Figure 1. (Top) Selected two-dimensional (2D) μGISAXS patterns (upper row, data; lower row, simulation) illustrate the evolution of key scattering features with increasing effective Au film thicknesses δ (left to right: 1.05 $\pm$ 0.02, 2.14 $\pm$ 0.04, 4.21 $\pm$ 0.09, 6.26 $\pm$ 0.13 nm). The arrows indicate the critical angles of the involved materials (orange, Au; blue, PS) in each image. The dark circles correspond to the specular beam stop used to prevent the detector from oversaturation. The black horizontal stripes correspond to the detector intermodular gaps. The coordinate system (q_y, q_z) and scale bars are indicated. (Bottom) Schematic drawings of gold cluster morphologies during sputter deposition on the PS/Si substrates illustrate different growth regimes: (I, green) nucleation and growth of isolated spherical islands; (II, blue) partial coalescence of hemispherical clusters; (III, magenta) coarsening of branched domains of flat spheroids; (IV, orange) continuous layer growth after percolation.

tional scattering feature points out that the growing nanostructures tend to arrange into larger domains in larger correlation distances during the deposition process. We are able to reproduce all of the above-mentioned key scattering features by simulating the scattering pattern based on a real-space model,[48] which we detail shortly below (for more details, see Supporting Information). An excellent agreement between data and simulation was obtained assuming a truncated sphere as particle shape with a variation of the cluster to surface contact angle CA from 120° at δ = 1.05 $\pm$ 0.02 nm, 80° at δ = 2.14 $\pm$ 0.04 nm, 70° at δ = 4.21 $\pm$ 0.09 nm, and 75° at δ = 6.26 $\pm$ 0.13 nm. The interparticle distance D was deduced from the maximum along q_y using the relation D $\approx 2\pi/q_{y,1,\max}$ to model side peak position (Figure S3, Supporting Information). Additional large domains using cylinder as particle shape are included for δ > 3 nm to simulate Yoneda broadening and respectively the second peak, $q_{y,2,\max}$.

Real-Time μGISAXS Analysis. To extract quantitative information from the sequence of μGISAXS patterns, out-of-plane cuts (along q_y) at the Yoneda peak position of PS (q_z = 0.69 nm^{-1}) and off-detector cuts (along q_z) for 0.187 nm^{-1} < q_y < 2.852 nm^{-1} were performed. Figure 2 shows contour plots of the out-of-plane and off-detector cuts versus the effective thickness δ of the deposited film. The detailed evolution of the above-mentioned key scattering features during the deposition process is clearly visible. The shift in side peak position ($q_{y,1,\max}$), the decrease of its full-width-at-half-maximum (Δ_1) extracted from Lorentzian fittings as well as the broadening of the Yoneda peak (Δ_{YON}) at q_y = 0 nm^{-1} and its related second side peak ($q_{y,2,\max}$) are depicted in Figure 2c (see also Figure S4, Supporting Information). A nonmonotonous shift of the side peak position toward lower q_y values was found indicating the existence of different growth regimes. In general, the shifting toward lower q_y is related to an increase in the average center-
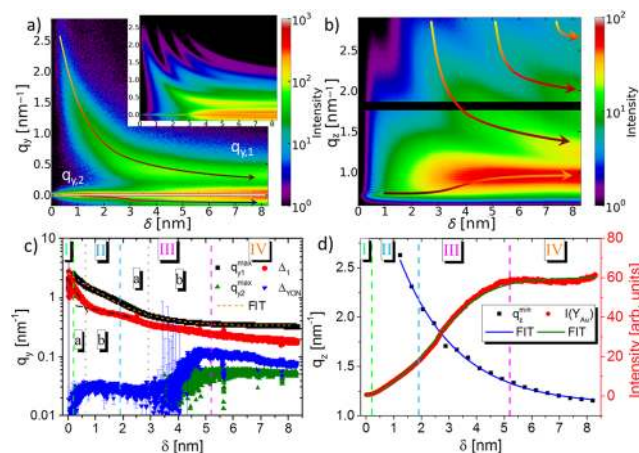

Figure 2. (a) Out-of-plane (along q_y) line cuts versus sputtered thickness at the PS Yoneda peak (q_z = 0.69 nm^{-1}). The arrows are guides to the eye showing exponential shift of primary peak position and the emerging of a new side peak next to the Yoneda peak around 3 nm thickness. The inset shows the corresponding map of the simulated sequence. (b) Off-detector (along q_z) line cuts versus thickness δ for 0.187 nm^{-1} < q_y < 2.852 nm^{-1}. The arrows indicate a sigmoidal shift between the critical angles during deposition and the shift of height modulations. (c) Evolution of the peak position ($q_{y,1,\max}$) and full-width-at-half-maximum of the main side peak (Δ_1), the Yoneda peak (Δ_{YON}) and the second side peak ($q_{y,2,\max}$). The dashed orange line is the exponential fit $q_{y,1,\max}(\delta)$ of the main peak position. The roman numerals represent individual growth regimes characterized by the predominant surface process: I, nucleation; II, isolated island growth with regimes IIa, diffusion mediated, and IIb, adsorption mediated; III, branched domain growth divided into IIIa, partial coalescence, and IIIb, coarsening; and IV, continuous layer growth. The vertical dashed lines indicate thresholds between individual growth regimes. (d) Evolution of the average intensity at the critical angle of Au ($I(Y_{\text{Au}})$) and the first-order minima along q_z ($q_{z,\min}$).

to-center distance, D, between Au clusters due to coalescence effects.[23,24] During the observed deposition process, the overall shift in the side peak position was approximated by an exponential decay plus offset (Figure 2c) $q_{y,1,\max}(\delta)$ = q_0 + A exp($-\delta/\delta_0$), with q_0 = 0.3346 $\pm$ 0.0004 nm^{-1}, A = 2.314 $\pm$ 0.007 nm^{-1}, and δ_0 = 1.151 $\pm$ 0.003 nm. This enabled us to track the mean cluster distance throughout the sputter deposition process using the relation D $\approx 2\pi/q_{y,1,\max}$. Because the width of the side peak is related to the mean cluster distance distribution, the observed decrease of Δ_1 reveals an increase in the order of the nanoclusters arrangement. The width of the Yoneda peak (Δ_{YON}) is related to diffuse scattering from surface roughness and the existence of larger domains observable at small scattering angles being not resolved in the μGISAXS setup. Figure 2d shows the evolution of the vertical scattering features in q_z direction as a function of effective film thickness. The first-order minima along $q_{z,\min}$ are directly connected to the height of truncated sphere shaped clusters in the framework of the oscillating behavior of the truncated sphere shaped form factor due to the first-order Bessel function.[48] To quantify the exponential shift, we extracted $q_{z,\min}$ for 15 effective film thicknesses δ from 1.3 to 8.3 nm in 0.5 nm steps and fitted with an exponential decay plus offset. The temporal evolution of the average intensity at the critical angle of Au, $I(Y_{\text{Au}})$, at q_z = 0.96 nm^{-1} is connected to variations of the electron density near the surface and can be interpreted
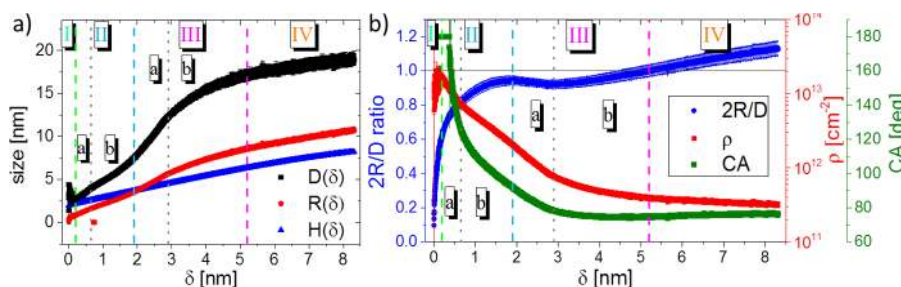
Figure 3. (a) Evolution of average real space parameters: (black) interparticle distance D, (red) cluster radius $R(\delta)$ and (blue) height $H(\delta)$ extracted independently by geometrical modeling.[24] (b) Evolution of morphological parameters (blue, cluster diameter over distance ratio $2R/D$; red, particle density (ρ); green, contact angle (CA)). The dashed lines indicate thresholds between individual growth regimes.

as an increase of the surface coverage or cluster density.[24] For instance, $I(Y_{Au})$ should not be fully developed before the percolation threshold has been reached. Basically, the intensity evolution can be well described by a Boltzmann sigmoidal function, in a manner similar to phase transition phenomena, indicating the transition from pristine PS/Si-substrate to a fully percolated gold layer.

At the very early stages of sputter deposition, we first observed an increase in the Yoneda peak width (Δ_{YON}), indicating an increase in roughness at the polymer surface due to nucleation and/or embedding of gold atoms. Furthermore, a shift of $q_{y,1,max}$ to higher values can be extracted, which is related to a decrease of cluster correlation distances during the nucleation process. After $\delta_I = 0.20 \pm 0.02$ nm, a transition from nucleation dominated to further cluster growth marks the nucleation threshold. Here, a continuous shift in peak position to lower q_y values due to the growth of small mobile clusters via diffusion-mediated coalescence is observed. As the deposition continued, a change in the slope of the Δ_1 was identified at $\delta_{II,a} = 0.65 \pm 0.05$ nm using linear interpolations (Figure 2c), indicating a transition in the growth kinetics from a predominant diffusion-mediated coalescence to an adsorption-mediated growth of immobilized cluster.[24] At $\delta_{II,b} = 1.90 \pm 0.11$ nm, Δ_1 shows a local maximum indicating the onset of a new growth regime. Here, a critical cluster size has been reached, where the time for two adjacent clusters to fully coalesce and to recover their shape exceeds the time for the clusters to grow due to deposition. Thus, the clusters partially coalesce and start forming elongated wormlike domains.[49,50] The associated reduction of the gold film roughness initially causes a slight decrease in the Yoneda peak width Δ_{YON}. With further deposition, the onset of further significant Yoneda peak broadening around $\delta_{III,a} = 2.90 \pm 0.17$ nm indicates the aggregation of the Au clusters into branched large domains. At this point, a second out-of-plane peak $q_{y,2,max}$ emerges from small q_y values to larger values related to a decrease in the correlation distances between the larger aggregates. The thin-film morphology becomes coarser until an effective thickness of $\delta_{III,b} = 5.2 \pm 0.3$ nm. Here, the evolution of the second peak $q_{y,2,max}$ levels off. The significantly retarded decrease in the main peak position $q_{y,1,max}$ and Δ_1 also point out that a critical interparticle distance has been reached, and lateral growth of individual clusters becomes further suppressed. Therefore, we identified this point as the percolation threshold, beyond which the Au clusters form large fractal-like interconnected domains on top of the PS. This is in accordance with the observed growth behavior of ultrathin Au films during sputter deposition on oxidized silicon substrates.[24]

Geometrical Modeling. Because μGISAXS provides averaged morphological information from all the objects within the X-ray footprint, the utilization of a simplified general geometrical model allows for extraction of average real space parameters from large sequences of in situ μGISAXS data. The model we propose assumes a local hexagonal arrangement of uniform hemispherical clusters, which are composed of the amount of material deposited on the unit cell surface area. This analytical tool supported the interpretation and evaluation of changes in cluster layer morphology derived from in situ μGISAXS data during gold sputter deposition according to size relationships between the model parameters.[24] Furthermore, the model was successfully applied to explain the correlation between nanostructure and Raman scattering enhancement for supported silver clusters in sensor applications.[25] In the present case, we apply it independently to $I(q_y)$ and $I(q_z)$ to decouple lateral and vertical size information, thus obtaining radius, distance, and height of the Au clusters, independently. Then, the main advantage is that the average cluster radius R can be calculated directly from the effective film thickness δ and the primary out-of-plane peak position $q_{y,1,max}$ according to[24]

$$R(\delta) = \sqrt[3]{\frac{3^{3/2}}{4\pi}D^2\delta} = \left[3^{3/2}\pi\frac{\delta}{q_{y,1,max}^2}\right]^{1/3} \tag{1}$$

Second, a comparison from the evolution of the minima along q_z in the data with the shift of $q_{z,min}$ minima in a set of simulated scattering patterns from defined growing hemispherical Au clusters allows in addition for independently extracting the average height H of model hemispheres decoupled from the above-mentioned radii (Figure S5, Supporting Information). Figure 3a shows the temporal evolution of the basic average real-space parameters, that is, interparticle distance D, hemispherical cluster radius $R(\delta)$ and height $H(\delta)$ as a function of effective film thickness δ. It can be clearly observed how the slope or curvature of the interparticle distance evolution changes significantly when crossing each indicated growth threshold. Initially, D is fast decreasing during nucleation (I), then fast increasing due to diffusion mediated coalescence of mobile isolated clusters (IIa), and its increase is decelerated due to mobility restrictions (IIb). With the onset of partial coalescence D increases again very fast (IIIa) until branching of the domains occurs (IIIb). After the percolation threshold (IV), the distance increases almost linearly, indicating layer growth. The evolution of decoupled particle height and radius allows for an important conclusion: on the basis of this model, we suggest a change in particle aspect ratio within the

first 3 nm deposition process and, later, a growth with nearly constant aspect ratio.

The aspect ratio deduced from the clusters' height and radius can be used to extract the average contact angle CA of the clusters, using following geometrical relationship:

$$CA(\delta) = \cos^{-1}\left(1 - \frac{H(\delta)}{R(\delta)}\right) \tag{2}$$

Another decisive advantage of the geometrical modeling is the calculation of the approximated average particle density ρ from the area covered by the model clusters within the triangular unit cell by[24]

$$\rho = \frac{2}{\sqrt{3}\,D^2} \tag{3}$$

Figure 3b shows the evolution of the ratio between in-plane diameter and distance $2R/D$ as the circular projection of noncircular 2D projected clusters, the particle density (ρ), and the contact angle (CA) deduced from the geometrical model. $2R/D$ increases continuously until the partial coalescence sets in at $\delta_{II,b}$ = 1.9 nm, where the course of $2R/D$ exhibits surprisingly a local maximum. Due to the onset of partial coalescence of previously isolated islands, the interparticle distance increases faster than the clusters grow, which leads to a release of initially covered surface area and significant faster decay in particle density. This phenomena has been predicted by Jeffers et al. during island-to-percolation transition during growth of metal films on nonwetting amorphous substrates.[49] The decrease reaches a local minimum at $\delta_{III,a}$ = 2.9 nm, where $2R/D$ increase again due to branching and coarsening of the elongated domains. In accordance with Jeffers et al., an absorption-mediated growth due to deposition overtakes the wiping due to coalescence and a metastable percolating cluster of connected islands is created.[49] Their kinetic freezing model was generally used to analyze the growth kinetics of metals on nonwetting surfaces.[40,45,51,52] The driving force of the diffusion limited partial coalescence is the reduction of the cluster curvature. As soon as the clusters reach a critical cluster size R_c, the time for two clusters to coalesce fully equals the time for one cluster to spread and touch its neighbors. Thus, the associated surface diffusion coefficient D_s at T = 296 K can be calculated by

$$D_s = \frac{k_b T J R_c^4}{\alpha \delta_c \gamma_{Au} \Omega^{4/3}} \tag{4}$$

where J = 0.49 ± 0.01 nm/min is the deposition rate, $\alpha \approx 1.035$ is the aspect ratio, γ_{Au} = 83 mJ/m^2 is the surface tension of sputter deposited gold,[40] and Ω = 1.69 × 10^{-29} m^3 the atomic volume of gold. Therefore, we can determine D_s = 7.33 × 10^{-18} m^2/s based on real-time in situ μGISAXS data using the critical cluster radius R_c ($\delta_c = \delta_{II,b}$) = 3.53 ± 0.09 nm derived from geometrical modeling. Ruffino et al. found D_s for Au on PS being in the same order of magnitude by extrapolating the onset of partial coalescence from atomic force microscopy images.[40] Furthermore, we can deduce the saturation density of nuclei N_0 = 1.6 × 10^{13} cm^{-2} and the related critical nucleus size R_c ($\delta_c = \delta_I$) = 0.87 ± 0.04 nm at the nucleation threshold. At the percolation threshold of $\delta_{III,b}$ = 5.2 nm the ratio $2R/D$ finally equals 1, so that the average clusters with $R_c(\delta_{III,b})$ = 8.52 ± 0.18 nm impinge on each other and form a fully percolated conductive gold film. This is in accordance with electrical

conductivity measurements on Au sputter deposited poly-(ethylene terephthalate) (PET) surfaces, where a decrease of more than 10 magnitudes in the sheet resistance was observed at effective Au layer thicknesses ranging from 4 to 6 nm.[53]

The quantitative results derived from geometrical modeling are in excellent agreement with the qualitative observation of the key scattering features (Figure 2). Especially, the initial prediction based on simulation from decreasing contact angles during deposition is preserved. In the beginning, we expect that the large cohesive energy of Au in conjunction with the very small Au-PS interaction energy gives rise to more spherical-shaped clusters. We may speculate that an incorporation of gold atoms in the polymer matrix by subsurface diffusion in the early stages changes the interfacial energy $\gamma_{Au/PS}$, and thus, contact angles below 180° are observed after δ = 0.38 ± 0.03 nm. With further deposition, the contact angles are further decreasing and reaching CA = 92 ± 1° at $\delta_{II,b}$ = 1.9 nm, where the onset of partial coalescence leads to the formation of elongated domains, and the growth regime of isolated islands ends. Afterward, the model contact angle approaches a constant value of CA = 75 ± 2° reflecting further cluster growth with similar aspect ratio. A similar decay in contact angles was reported previously from Grachev et al. during sputter deposition of silver on alumina substrates, where the particle form changes from truncated spheres with CA > 140° to truncated oblate spheroids within the first 3.0 nm deposited film thickness.[45]

By knowing the contact angle of the Au clusters, one can estimate the interfacial energy between the Au and the PS thin film $\gamma_{Au/PS}$ by applying the Young−Dupré equation:

$$\cos CA = \frac{\gamma_{PS} - \gamma_{Au/PS}}{\gamma_{Au}} \tag{5}$$

where CA is the contact angle, and γ_{Au} and γ_{PS} are the surface energies of the Au film and PS substrate, respectively. According to the static contact angle measurements of Ruffino et al., the surface free energy of spin coated PS thin films is γ_{PS} = 31 ± 3 mJ/m^2 and the surface free energy of sputtered Au thin films is γ_{Au} = 83 ± 6 mJ/m^2.[40] Thus, for a contact angle of CA = 75 ± 2°, the interfacial energy between Au clusters and PS thin films can be estimated as $\gamma_{Au/PS}$ = 10 ± 5 mJ/m^2, whereas Ruffino et al. deduced 14 ± 8 mJ/m^2.[40] We believe that the use of different polymers and/or metals may change the evolution of nanoparticle contact angles during sputter deposition and may promote the fabrication of truncated nanospheres.

Growth Morphology and Depth Profile. To further corroborate the observed changes in thin film morphology during the different stages of growth, we show FESEM images at different film thicknesses in Figure 4. At δ = 2.1 nm isolated spherical island are visible and few of them already start to form
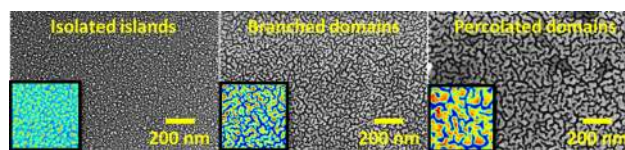

Figure 4. FESEM images at different film thicknesses showing stages of growth: from left to right: start of partial coalescence of isolated islands at 2.1 nm; branched domains at 4.2 nm; percolated gold domains at 6.3 nm. The insets show 400 × 400 nm area in false color representation.

elongated aggregations due to partial coalescence. They tend to grow further into branched domains at 4.2 nm, and at 6.3 nm percolated domains are clearly visible. At all intermediate steps, the domains still consist of smaller clusters (insets), which are responsible for the primary out-of-plane scattering feature $q_{y,1,max}$.

For further investigating the depth profile of the established Au film, X-ray reflectivity (XRR) measurements were performed in situ before ($\delta_{Au} = 0$ nm) and after ($\delta_{Au} = 8.31 \pm 0.17$ nm) completed deposition. Because the X-rays can penetrate thin Au films and the difference in electron density between PS and Au is rather large, this measurement enables the detection of small gold incorporations in the near surface region of the metal−polymer interface. The reflectivity data of the pristine PS film was fitted to a model representing a rough 0.4 nm thick native SiO_2 layer with $\sigma_{rms} = 1.0$ nm covered by a 91.3 ± 1.2 nm thick PS layer with $\sigma_{rms} = 1.3$ nm roughness on a silicon substrate (Figure 5a). After deposition, an excellent
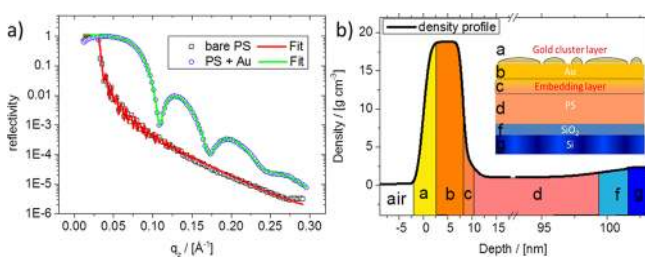

Figure 5. XRR measurements (a) directly before (black rectangle/red line) and after 1012 s Au sputter deposition (blue circle/green line) suggesting a (b) density profile consisting of five layers (inlet) Si/ SiO_2/PS/AuPS/Au/air including a rough gold cluster layer and an embedding layer appearing as weak shoulder in the density profile.

agreement between XRR data and fit was obtained assuming a five-layer model Si/SiO_2/PS/AuPS/Au/air as depicted in Figure 5b. It consists of an 8.1 ± 0.3 nm thick layer with 97% of bulk Au density and $\sigma_{rms} = 1.1$ nm roughness to model the gold cluster layer. An additional 2.2 nm thick layer with 23% of bulk Au density and 0.6 ± 0.2 nm interface roughness was introduced between Au and PS. Due to the relatively short time delay between deposition well below PS glass transition temperature and the in situ XRR measurement, thermodynamic subsurface diffusion of Au clusters into the polymer matrix is considered to be negligible. It is supposed to occur on much longer time scales, even at temperatures well above PS glass transition.[54] Therefore, the observed enrichment layer can be most likely associated with an embedding of isotropically diffusing adatoms or small clusters during the early stages of deposition. Later on, mobile larger sized particles adsorb further deposited adatoms, inducing a surface metal enrichment and the strong aggregation tendency impedes the embedding process.[55] Hence, Kaune et al. observed a 1.2 nm gold enrichment layer with 12% of bulk Au density after stepwise DC/magnetron sputter deposition at higher deposition rates on a poly(9-vinylcarbazole) thin film using XRR method.[23] Both results match the prediction of a 1−2 nm embedding layer in depth-resolved concentration profiles derived from the kinetic Monte Carlo simulation of noble metal growth on polymers at different deposition rates.[56] The differences in embedding behavior suggest on the one hand a strong dependency on the applied sputter deposition parameters, such as deposition rates or bias-voltage.[55] On the other hand, physicochemical metal−

polymer interactions at the interface also expose strong influence on embedding dynamics, which could be tuned with the temperature, chemical composition of the polymer chains, and their radius of gyration.[57,58] Possible subsurface diffusion of noble metal atoms in polymer films even at room temperature has been reported by Thran et al.[59] and by Metwalli et al.[22] on 3D gold decoration of embedded PS domains. Furthermore, we may speculate that a higher roughness of the polymer thin film has influence on the saturation density of nuclei N_0 and the related critical nucleus size R_c at the nucleation threshold.[19] Moreover, the onset of partial coalescence could be shifted to higher effective thicknesses due to more pronounced height differences on the substrate. Similarly, higher deposition rates could affect the cluster growth kinetics in the early stages, where the higher adatom density promotes nucleation and diffusion-mediated cluster growth. A pronounced shift in the percolation threshold is not expected because the cluster growth is dominated by adsorption processes in the later stages.

Real-Time Specular Reflectance Spectroscopy. Apart from the fundamental aspects of Au growth on PS, the changes in the optical properties induced by metal nanoparticle growth during the sputter deposition process were exemplarily monitored using specular reflectance spectroscopy (SRS) in the UV/vis range.[44,45] This method was successfully applied to quantify the growth of silver nanoclusters on alumina substrates during sputter deposition.[45] The relative UV/vis reflectance signal $r_\%$ as a function of the optical wavelength λ_{opt} is represented by

$$[r_\%(\lambda_{opt}, \delta)] = \frac{r(\delta)}{r_0} \times 100 \tag{6}$$

where r_0 is the background and $r(\delta)$ is the reflectivity of the Au covered sample with layer thickness δ. Since we consider the ratio of the reflectivity to the pristine PS thin film r_0, only intensity fluctuations due to the deposition process and particle growth contribute to the SRS signal. Figure 6a shows the evolution of the wavelength dependent reflectivity signal $r_\%$ (λ_{opt}, δ) as a function of effective layer thickness during the Au deposition on PS thin films using same conditions as during the
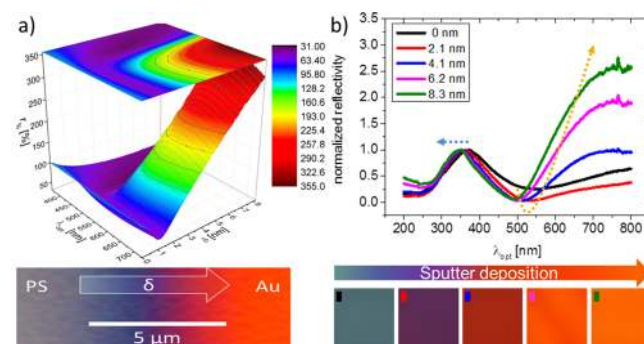

Figure 6. Change in optical properties during the deposition process presented as (a, top) SRS data as a function of wavelength λ_{opt} and effective thickness δ and (bottom) optical microscopic image of a 5 μm gradient exposing all thin film colors during deposition. (b, Top) UV/vis-reflectivity spectra of as-prepared PS films at different Au film thicknesses. The arrows are guides to the eye showing the blue shift of polymer reflectance and red shift of optical reflectance. (b, Bottom) visible color from optical microscopy at different film thicknesses (scale bar 20 μm).

μGISAXS experiment. Starting with a constant line of 100%, the averaged relative reflectivity in the complete inspected spectral range $\langle r_\% \rangle$ decreases very fast within the early stages and reaches a local region of $\langle r_\% \rangle \approx 55\%$ between $\delta = 0.85$ and 1.05 nm (Figure S9, Supporting Information). The decrease in specular reflectivity can be associated with the increase of surface roughness due to the deposition/embedding of Au adatoms and growth of small isolated nanoparticles at the polymer surface.[60] After the deposition of an effective gold layer thickness of $\delta = 2.67$ nm, the average reflectivity increases continuously and reaches again 100% for wavelengths higher than 530 nm, which is around the typical surface plasmon resonance (SPR) band of gold clusters.[61] For wavelengths smaller than 530 nm, the reflectance is further decreasing due to absorption resulting in a change in color from blue to red thin films. With progressively deposition beyond the onset of partial coalescence at $\delta_{II,b} = 1.9$ nm, a linear increase in average reflectivity with a slope of $\Delta \langle r_\% \rangle / \Delta \delta = 31\%/$nm can be extracted (Figure S9, Supporting Information). In addition, a red shift and broadening of a local maximum connected to changes in SPR frequencies is visible, which indicates the growth and aggregation of nanoparticles. Thus, the resulting PS film covered with 8.3 nm Au reaches a relative reflectivity of $r_\% = 350\%$ at 620 nm.

It is well-known that the characteristic localized reflectivity of nanostructured gold films is very sensitive to the surrounding medium, particle size, surface structure, and shape.[4,6,62,63] In particular, Gulan and Turan showed on a variety of nanosized gold arrays produced by electron-beam lithography that a red shift in optical reflectance spectra occurs with increasing particle size and interparticle distance. In our case, the size and distance of truncated-sphere-shaped particles are initially increasing within a polymer-rich environment. With the onset of formation of branched domains at $\delta_{III,a} = 2.90 \pm 0.17$ nm the optical reflectivity is dominated by larger aggregates, where transverse and longitudinal SPR oscillation modes are possible, and the environment is metal enriched. Therefore, the explanation of optical reflectivity data solely based on SPR effects should be carefully handled, since changes in size, shape, and environment are continuously occurring upon metal upload.[6] Figure 6a shows also an optical microscope image of a 5 μm gradient sample produced with a sharped-edged silicon-wafer as deposition mask. All the thin film colors induced by Au deposition are visible in this gradient. The pristine gray-blue PS film initially becomes dark blue and changes its color from violet over amber to orange with further deposition.

UV/vis-reflectivity spectra and optical microscopic images of the as-prepared PS films at different Au film thicknesses illustrate the same tendency (Figure 6b). The pristine PS thin films show a local maximum around $\lambda_{opt} = 372 \pm 1$ nm stemming from interference due to multiple reflections at the correlated polymer/substrate and air/polymer interface. Thus, the position of this peak depends on PS film thickness, refractive index, and incident angle.[44,64] To better compare the effect of Au deposition on the reflectivity, we normalized the spectra to this peak.

At an Au thickness of $\delta = 2.1$ nm, the initially significant peak shifts to $\lambda_{opt} = 353$ nm, which can be attributed to a change in effective refractive index at the metal–polymer interface due to embedding of gold atoms and growth of supported nano-clusters. With ongoing deposition, this peak shifts in wavelength only by $\Delta \lambda_{opt} / \Delta \delta = 0.5$, indicating vertical layer growth. Another striking point is that the specular reflectivity of visible

light (λ_{opt} from 400 to 700 nm) is lower compared to the pristine PS substrate. Here, the formation of small clusters at the polymer interface may lead to interference effects and thus enhances the diffuse reflectance. This antireflective phenomena was also reported by Gompf et al. in the infrared region for nanometer thick gold layers on silicon.[65] They reported $\delta = 3$ nm as a threshold for this abnormal behavior, which is in good agreement with the $\delta_{III,a} = 2.90 \pm 0.17$ thickness from the in situ μGISAXS data and might be thus connected to the formation of larger branched Au aggregates.

■ CONCLUSIONS

The investigated preparation of homogeneous metal–polymer nanocomposites by sputter deposition of Au on PS thin films matches the primary challenge of nanotechnology for reproducible, low-cost fabrication with tailored optical properties over a large area. From the combination of in situ time-resolved μGISAXS and in situ SRS measurements during sputter deposition, the impact on optoelectronic properties can be tracked and related to the nanostructural evolution of gold cluster morphology. In particular, the prepared Au/PS nanocomposite thin films at different thicknesses exhibited significant changes in their morphology, optoelectronic properties, and visible color. The observed antireflective behavior with its maximum at 0.95 ± 0.1 nm thickness suggests a promising range for effective resonant cluster layers in OPV applications to increase their light harvesting capabilities. Moreover, the adjustable optical thin film properties induced by the cluster layer can be applied to tune the optical response of functional polymer surfaces or anticounterfeiting security features.[5] On the basis of our findings, we believe that our study opens up the possibility to tune the size of the interparticle gap and the perimeter of supported nanoparticles, which is mandatory for creating hot-spots in SERS applications or active binding sites in heterogeneous catalysis. A maximum in SERS activity of sputtered Ag clusters on silicon wafers was found for average interparticle gaps of 0.9 nm,[25] which occurs in the given investigation at effective thicknesses around 3.2 ± 0.5 nm. We also speculate that a maximum of catalytic activity should be available for thickness below $\delta_{II,b} = 1.9$ nm, because partial coalescence strongly reduces the amount of accessible binding sites at the clusters boundaries. Furthermore, a gold layer of 6–8 nm thickness should be sufficient to install a conductive gold layer as, for example, gate or drain electrodes in OFETs applications.

In addition, XRR confirms the observation of an embedded Au layer during the deposition resulting in a 2.3 nm gold enrichment layer with 23% of bulk Au density. We speculate that only individual atoms are responsible for this layer, because the embedding of gold nanoparticles in PS thin films is thermodynamically favored at elevated temperatures.[57] Because it is known that the incorporation of metal atoms in organic thin films can induce charge transfer phenomena resulting in enhanced electron injections,[66] sputter deposition under optimized conditions will play a key role to selectively dope metal–organic interfaces and to adjust their optoelectronic properties for specified applications.[63] This holds true especially for the efficiency of OPV devices, where supported noble metal nanoparticles enhance the photovoltaic conversion[10] or, embedded in the active layer, act as performance stabilizers to reduce the photodegradation rate.[11]

In summary, the obtained detailed information is highly relevant for adjusting the nanostructured Au morphology at

metal–polymer interfaces with tailored absorption and reflectance behavior in the UV/vis range via sputter deposition for plasmonic-enhanced sensors, OFETs, OPVs, and OLEDs, for example.

EXPERIMENTAL SECTION

μGISAXS was performed at the P03/MiNaXS beamline of the PETRA III storage ring at DESY (Hamburg, Germany).[67,68] A highly automated radio frequency (RF) sputter chamber[46] was integrated in the μGISAXS setup to enable in situ and real-time observations of morphological evolution. An incident photon energy of 13 keV with a beam size of $31 \times 24\ \mu m^2$ at the sample position was used. The sample to detector distance was set at SDD = 1836 ± 2 mm and a PILATUS 300 K (Dectris Ltd., Switzerland) with a pixel size of $172 \times 172\ \mu m^2$ was used as detector. The sputter deposition experiments were performed onto 91 ± 5 nm thin polystyrene films (PS280, M_w = 280 kg/mol, Sigma-Aldrich, UK) obtained by spin coating from 13.1 g/L polymer solution in toluene onto previously acid-cleaned Si substrates (Supporting Information). Further details about the sputter source and geometry can be found elsewhere.[46] To achieve a good separation between the PS and Au Yoneda peaks, we used an incident angle of α_i = 0.5° during the in situ experiment. Sputter deposition was performed for 1012 s using a plasma-cleaned 99.999% Au target (Kurt J. Lesker, Germany) and a sputter power of 100 W at an Ar working pressure of 1.5×10^{-2} mbar. To avoid possible X-ray beam damage during the in situ μGISAXS experiment on the sample, we performed repeated scanning along the sample in the horizontal direction.[36] Meanwhile, the scattering patterns were continuously recorded at a frame rate of 10 images per second. The final Au effective thickness δ_{Au} = 8.31 ± 0.17 nm was determined from a static μGISAXS image recorded directly after deposition which results in an effective deposition rate of J = 0.49 ± 0.01 nm/min. The thicknesses of the pure PS layer and the final Au layer were alternatively determined from two-dimensional X-ray reflectivity (XRR) measurements before and after the in situ μGISAXS experiment by fitting the specular reflection projected on the PILATUS 300 K using a 2D Gaussian. Hereby, the incidence angle (α_i) was scanned from 0.05 to 1.25° in three intervals with different aluminum attenuators to prevent detector saturation and at two different detector positions in the z direction to avoid shadowing from intermodular detector gaps. The μGISAXS data were analyzed using the DPDAK software package.[69] XRR fitting and density profile was done using pyXRR software.

For additional in situ measurement of the optical properties, the sputter chamber was equipped with an UV/vis spectrometer (Andor, UK) operating under an incident angle of α_{inc} = 53.47° to enable in situ specular reflectivity measurements in the UV/vis regime. During 1000 s of sputter deposition under exactly the same conditions as mentioned above, full SRS spectra ranging from 362 to 727 nm were recorded every second from the sample center on a focused spot size of about $0.5 \times 0.5\ mm^2$ using 50 accumulations of 0.02 s.

Intermediate samples were produced with δ = 2.1, 4.2, and 6.3 nm effective thickness using same preparation parameters as above and were subsequently analyzed via static μGISAXS at two different incident angles of α_i = 0.5 and 0.25° to increase the surface sensitivity. The samples were further characterized with FESEM, XPS, UV/vis (ranging from 200 to 800 nm) and optical microscopy (Keyence, Japan). Field emission scanning electron microscopy (FESEM) images were obtained with an NVision 40 (Carl Zeiss SMT, Germany) at a low working distance of 3.0 mm with an accelerating voltage of 5 kV. Simulations were performed with IsGISAXS software V2.6 for comparison with the μGISAXS data.[48] See Supporting Information for more details.

ASSOCIATED CONTENT

$\mathbf{S}$ Supporting Information

Full μGISAXS image sequence of the experiment as movie file; μGISAXS geometry, static GISAXS data, real-time μGISAXS data analysis, IsGISAXS simulation, ellipsometry, UV/vis specular reflectance spectroscopy, and X-ray photoelectron spectroscopy. The Supporting Information is available free of charge on the ACS Publications website at DOI: 10.1021/acsami.5b02901.

AUTHOR INFORMATION

Corresponding Author
*Tel.: +4940/8998-3768. E-mail: Matthias.Schwartzkopf@desy.de.

Present Address
‖Instituto de Ciencia de Materiales de Madrid, CSIC, Sor Juana Inés de la Cruz 3, Cantoblanco, E-28049 Madrid, Spain.

Notes
The authors declare no competing financial interest.

ACKNOWLEDGMENTS

REFERENCES

(1) Whitesides, G. M.; Grzybowski, B. Self-Assembly at All Scales. *Science* **2002**, *295*, 2418–2421.

(2) Lehn, J.-M. Toward Self-Organization and Complex Matter. *Science* **2002**, *295*, 2400–2403.

(3) Pyykkö, P. Theoretical Chemistry of Gold. *Angew. Chemie, Int. Ed.* **2004**, *116*, 4512–4557.

(4) Walter, H.; Bauer, G.; Domnick, R.; Jakopic, G.; Leitner, A. Role of Granular Structure in Metal Layers on the Optical Properties of Absorbing Mirrors. *Opt. Eng.* **2006**, *45*, 103801.

(5) Bauer, G.; Hassmann, J.; Walter, H.; Haglmüller, J.; Mayer, C.; Schalkhammer, T. Resonant Nanocluster Technology—From Optical Coding and High Quality Security Features to Biochips. *Nanotechnology* **2003**, *14*, 1289–1311.

(6) Guler, U.; Turan, R. Effect of Particle Properties and Light Polarization on the Plasmonic Resonances in Metallic Nanoparticles. *Opt. Express* **2010**, *18*, 17322–17338.

(7) Cho, E. C.; Au, L.; Zhang, Q.; Xia, Y. The Effects of Size, Shape, and Surface Functional Group of Gold Nanostructures on Their Adsorption and Internalization by Cells. *Small* **2010**, *6*, 517–522.

(8) Nie, X.; Qian, H.; Ge, Q.; Xu, H.; Jin, R. CO Oxidation Catalyzed by Nanoclusters and Identification of Perimeter Sites as Active Centers. *ACS Nano* **2012**, *6*, 6014–6022.

(9) Green, I.; Tang, W.; Neurock, M.; Yates, J. Spectroscopic Observation of Dual Catalytic Sites during Oxidation of CO on a Au/TiO$_2$ Catalyst. *Science* **2011**, *333*, 736–739.

(10) Westphalen, M.; Kreibig, U.; Rostalski, J.; Lu, H.; Meissner, D. Metal Cluster Enhanced Organic Solar Cells. *Sol. Energy Mater. Sol. Cells* **2000**, *61*, 97–105.

(11) Paci, B.; Generosi, A.; Albertini, V. R.; Spyropoulos, G. D.; Stratakis, E.; Kymakis, E. Enhancement of Photo/Thermal Stability of Organic Bulk Heterojunction Photovoltaic Devices via Gold Nanoparticles Doping of the Active Layer. *Nanoscale* **2012**, *4*, 7452–7459.

(12) Wu, J.-L.; Chen, F.-C.; Hsiao, Y.-S.; Chien, F.-C.; Chen, P.; Kuo, C.-H.; Huang, M. H.; Hsu, C.-S. Surface Plasmonic Effects of Metallic Nanoparticles on the Performance of Polymer Bulk Heterojunction Solar Cells. *ACS Nano* **2011**, *5*, 959–967.

(13) Faupel, F.; Zaporojtchenko, V.; Strunskus, T.; Elbahri, M. Metal-Polymer Nanocomposites for Functional Applications. *Adv. Eng. Mater.* **2010**, *12*, 1177−1190.

(14) Müller-Buschbaum, P. The Active Layer Morphology of Organic Solar Cells Probed with Grazing Incidence Scattering Techniques. *Adv. Mater.* **2014**, 7692−7709.

(15) Yamashita, Y. Organic Semiconductors for Organic Field-Effect Transistors. *Sci. Technol. Adv. Mater.* **2009**, *10*, 024313.

(16) Huang, W.; Yu, X.; Fan, H.; Yu, J. High Performance Unipolar Inverters by Utilizing Organic Field-Effect Transistors with Ultraviolet/Ozone Treated Polystyrene Dielectric. *Appl. Phys. Lett.* **2014**, *105*, 093302.

(17) Burroughes, J.; Bradley, D.; Brown, A. Light-Emitting Diodes Based on Conjugated Polymers. *Nature* **1990**, *347*, 539−541.

(18) Hobson, P. A.; Wedge, S.; Wasey, J. A. E.; Sage, I.; Barnes, W. L. Surface Plasmon Mediated Emission from Organic Light-Emitting Diodes. *Adv. Mater.* **2002**, *14*, 1393−1396.

(19) Venables, J. A.; Spiller, G. D. T.; Hanbücken, M. Nucleation and Growth of Thin Films. *Rep. Prog. Phys.* **1984**, *47*, 399−459.

(20) Zhang, Z.; Lagally, M. G. Atomistic Processes in the Early Stages of Thin-Film Growth. *Science* **1997**, *276*, 377−383.

(21) Levine, J. R.; Cohen, J. B.; Chung, Y. W.; Georgopoulos, P. Grazing-Incidence Small-Angle X-Ray Scattering: New Tool for Studying Thin Film Growth. *J. Appl. Crystallogr.* **1989**, *22*, 528−532.

(22) Metwalli, E.; Couet, S.; Schlage, K.; Röhlsberger, R.; Körstgens, V.; Ruderer, M.; Wang, W.; Kaune, G.; Roth, S. V.; Müller-Buschbaum, P. In Situ GISAXS Investigation of Gold Sputtering onto a Polymer Template. *Langmuir* **2008**, *24*, 4265−4272.

(23) Kaune, G.; Ruderer, M. A.; Metwalli, E.; Wang, W.; Couet, S.; Schlage, K.; Röhlsberger, R.; Roth, S. V.; Müller-Buschbaum, P. In Situ GISAXS Study of Gold Film Growth on Conducting Polymer Films. *ACS Appl. Mater. Interfaces* **2009**, *1*, 353−360.

(24) Schwartzkopf, M.; Buffet, A.; Körstgens, V.; Metwalli, E.; Schlage, K.; Benecke, G.; Perlich, J.; Rawolle, M.; Rothkirch, A.; Heidmann, B.; et al. From Atoms to Layers: In Situ Gold Cluster Growth Kinetics during Sputter Deposition. *Nanoscale* **2013**, *5*, 5053−5062.

(25) Santoro, G.; Yu, S.; Schwartzkopf, M.; Zhang, P.; Koyiloth Vayalil, S.; Risch, J. F. H.; Rübhausen, M. A.; Hernández, M.; Domingo, C.; Roth, S. V. Silver Substrates for Surface Enhanced Raman Scattering: Correlation between Nanostructure and Raman Scattering Enhancement. *Appl. Phys. Lett.* **2014**, *104*, 243107.

(26) Yu, S.; Santoro, G.; Sarkar, K.; Dicke, B.; Wessels, P.; Bommel, S.; Döhrmann, R.; Perlich, J.; Kuhlmann, M.; Metwalli, E.; et al. Formation of Al Nanostructures on Alq3: An in Situ Grazing Incidence Small Angle X-Ray Scattering Study during RF Sputter Deposition. *J. Phys. Chem. Lett.* **2013**, *4*, 3170−3175.

(27) Bommel, S.; Kleppmann, N.; Weber, C.; Spranger, H.; Schäfer, P.; Novak, J.; Roth, S. V.; Schreiber, F.; Klapp, S. H. L.; Kowarik, S. Unravelling the Multilayer Growth of the Fullerene C60 in Real Time. *Nat. Commun.* **2014**, *5*, 5388.

(28) Roth, S. V.; Herzog, G.; Körstgens, V.; Buffet, A.; Schwartzkopf, M.; Perlich, J.; Abul Kashem, M. M.; Döhrmann, R.; Gehrke, R.; Rothkirch, A.; et al. In Situ Observation of Cluster Formation during Nanoparticle Solution Casting on a Colloidal Film. *J. Phys.: Condens. Matter* **2011**, *23*, 254208.

(29) Al-Hussein, M.; Schindler, M.; Ruderer, M. a; Perlich, J.; Schwartzkopf, M.; Herzog, G.; Heidmann, B.; Buffet, A.; Roth, S. V.; Müller-Buschbaum, P. In Situ X-Ray Study of the Structural Evolution of Gold Nano-Domains by Spray Deposition on Thin Conductive P3HT Films. *Langmuir* **2013**, *29*, 2490−2497.

(30) Perlich, J.; Schwartzkopf, M.; Körstgens, V.; Erb, D.; Risch, J. F. H.; Müller-Buschbaum, P.; Röhlsberger, R.; Roth, S. V.; Gehrke, R. Pattern Formation of Colloidal Suspensions by Dip-Coating: An in Situ Grazing Incidence X-Ray Scattering Study. *Phys. Status Solidi RRL* **2012**, *6*, 253−255.

(31) Schell, N.; Pagh Andreasen, K.; Bøttiger, J.; Chevallier, J. On the Dependence on Bias Voltage of the Structural Evolution of Magnetron- Sputtered Nanocrystalline Cu Films during Thermal Annealing. *Thin Solid Films* **2005**, *476*, 280−287.

(32) Krause, B.; Darma, S.; Kaufholz, M.; Gräfe, H. H.; Ulrich, S.; Mantilla, M.; Weigel, R.; Rembold, S.; Baumbach, T. Modular Deposition Chamber for in Situ X-Ray Experiments during RF and DC Magnetron Sputtering. *J. Synchrotron Radiat.* **2012**, *19*, 216−222.

(33) Krause, M.; Buljan, M.; Mücklich, A.; Möller, W.; Fritzsche, M.; Facsko, S.; Heller, R.; Zschornak, M.; Wintz, S.; Endrino, J. L.; et al. Compositionally Modulated Ripples during Composite Film Growth: Three-Dimensional Pattern Formation at the Nanoscale. *Phys. Rev. B* **2014**, *89*, 085418.

(34) Metwalli, E.; Körstgens, V.; Schlage, K.; Meier, R.; Kaune, G.; Buffet, A.; Couet, S.; Roth, S. V.; Röhlsberger, R.; Müller-Buschbaum, P. Cobalt Nanoparticles Growth on a Block Copolymer Thin Film: A Time-Resolved GISAXS Study. *Langmuir* **2013**, *29*, 6331−6340.

(35) Schlage, K.; Couet, S.; Roth, S. V.; Vainio, U.; Rüffer, R.; Abul Kashem, M. M.; Müller-Buschbaum, P.; Röhlsberger, R. The Formation and Magnetism of Iron Nanostructures on Ordered Polymer Templates. *New J. Phys.* **2012**, *14*, 043007.

(36) Yu, S.; Santoro, G.; Yao, Y.; Babonneau, D.; Schwartzkopf, M.; Zhang, P.; Vayalil, S. K.; Wessels, P.; Döhrmann, R.; Drescher, M.; et al. Following the Island Growth in Real Time: Ag Nanocluster Layer on Alq3 Thin Film. *J. Phys. Chem. C* **2015**, *119*, 4406−4413.

(37) Sun, Y.; Xia, Y. Shape-Controlled Synthesis of Gold and Silver Nanoparticles. *Science* **2002**, *298*, 2176−2179.

(38) Amarandei, G.; O'Dwyer, C.; Arshak, A.; Corcoran, D. Fractal Patterning of Nanoparticles on Polymer Films and Their SERS Capabilities. *ACS Appl. Mater. Interfaces* **2013**, *5*, 8655−8662.

(39) Lopes, W.; Jaeger, H. Hierarchical Self-Assembly of Metal Nanostructures on Diblock Copolymer Scaffolds. *Nature* **2001**, *414*, 735−738.

(40) Ruffino, F.; Torrisi, V.; Marletta, G.; Grimaldi, M. G. Growth Morphology of Nanoscale Sputter-Deposited Au Films on Amorphous Soft Polymeric Substrates. *Appl. Phys. A: Mater. Sci. Process.* **2011**, *103*, 939−949.

(41) Roth, S. V.; Santoro, G.; Risch, J. F. H.; Yu, S.; Schwartzkopf, M.; Boese, T.; Do, R.; Zhang, P.; Besner, B.; Bremer, P.; et al. Patterned Diblock Co-Polymer Thin Films as Templates for Advanced Anisotropic Metal Nanostructures. *ACS Appl. Mater. Interfaces* **2015**, DOI: 10.1021/am507727f.

(42) Amarandei, G.; Dwyer, C. O.; Arshak, A.; Thiele, U.; Steiner, U.; Corcoran, D. Effect of Au Nanoparticle Spatial Distribution on the Stability of Thin Polymer Films. *Langmuir* **2013**, *29*, 6706−6714.

(43) Mukherjee, R.; Das, S.; Das, A.; Sharma, S. K.; Raychaudhuri, A. K.; Sharma, A. Stability and Dewetting of Metal Nanoparticle Filled Thin Polymer Films: Dynamics. *ACS Nano* **2010**, *4*, 3709−3724.

(44) McIntyre, J.; Aspnes, D. Differential Reflection Spectroscopy of Very Thin Surface Films. *Surf. Sci.* **1971**, *24*, 417−434.

(45) Grachev, S.; de Grazia, M.; Barthel, E.; Søndergård, E.; Lazzari, R. Real-Time Monitoring of Nanoparticle Film Growth at High Deposition Rate with Optical Spectroscopy of Plasmon Resonances. *J. Phys. D. Appl. Phys.* **2013**, *46*, 375305.

(46) Döhrmann, R.; Botta, S.; Buffet, A.; Santoro, G.; Schlage, K.; Schwartzkopf, M.; Bommel, S.; Risch, J. F. H.; Mannweiler, R.; Brunner, S.; et al. A New Highly Automated Sputter Equipment for in Situ Investigation of Deposition Processes with Synchrotron Radiation. *Rev. Sci. Instrum.* **2013**, *84*, 043901.

(47) Babonneau, D.; Camelio, S.; Lantiat, D.; Simonot, L.; Michel, A. Waveguiding and Correlated Roughness Effects in Layered Nanocomposite Thin Films Studied by Grazing-Incidence Small-Angle X-Ray Scattering. *Phys. Rev. B: Condens. Matter Mater. Phys.* **2009**, *80*, 1−12.

(48) Lazzari, R. IsGISAXS: A Program for Grazing-Incidence Small-Angle X-Ray Scattering Analysis of Supported Islands. *J. Appl. Crystallogr.* **2002**, *35*, 406−421.

(49) Jeffers, G.; Dubson, M. A.; Duxbury, P. M. Island-to-Percolation Transition during Growth of Metal Films. *J. Appl. Phys.* **1994**, *75*, 5016−5020.

(50) Lim, T.; McCarthy, D.; Hendy, S.; Stevens, K. J.; Brown, S. A.; Tilley, R. D. Real-Time TEM and Kinetic Monte Carlo Studies of the Coalescence of Decahedral Gold Nanoparticles. *ACS Nano* **2009**, *3*, 3809−3813.

(51) Zhang, L.; Cosandey, F.; Persaud, R.; Madey, T. Initial Growth and Morphology of Thin Au Films on TiO_2(110). *Surf. Sci.* **1999**, *439*, 73−85.

(52) Chinta, P. V.; Headrick, R. L. Bimodal Island Size Distribution in Heteroepitaxial Growth. *Phys. Rev. Lett.* **2014**, *112*, 2−5.

(53) Švorčík, V.; Slepička, P.; Švorčíková, J.; Špírková, M.; Zehentner, J.; Hnatowicz, V. Characterization of Evaporated and Sputtered Thin Au Layers on Poly(ethylene terephtalate). *J. Appl. Polym. Sci.* **2006**, *99*, 1698−1704.

(54) Amarandei, G.; O'Dwyer, C.; Arshak, A.; Corcoran, D. The Stability of Thin Polymer Films as Controlled by Changes in Uniformly Sputtered Gold. *Soft Matter* **2013**, *9*, 2695−2702.

(55) Faupel, F.; Willecke, R.; Thran, A. Diffusion of Metals in Polymers. *Mater. Sci. Eng. R Reports* **1998**, *22*, 1−55.

(56) Rosenthal, L.; Filinov, A.; Bonitz, M.; Zaporojtchenko, V.; Faupel, F. Diffusion and Growth of Metal Clusters in Nanocomposites: A Kinetic Monte Carlo Study. *Contrib. Plasma Phys.* **2011**, *51*, 971−980.

(57) Amarandei, G.; Clancy, I.; O'Dwyer, C.; Arshak, A.; Corcoran, D. Stability of Ultrathin Nanocomposite Polymer Films Controlled by the Embedding of Gold Nanoparticles. *ACS Appl. Mater. Interfaces* **2014**, *6*, 20758−20767.

(58) Zaporojtchenko, V.; Behnke, K.; Thran, A.; Strunskus, T.; Faupel, F. Condensation Coefficients and Initial Stages of Growth for Noble Metals Deposited onto Chemically Different Polymer Surfaces. *Appl. Surf. Sci.* **1999**, *144−145*, 355−359.

(59) Thran, A.; Strunskus, T.; Zaporojtchenko, V.; Faupel, F. Evidence of Noble Metal Diffusion in Polymers at Room Temperature and Its Retardation by a Chromium Barrier. *Appl. Phys. Lett.* **2002**, *81*, 244−246.

(60) Hunderi, O. Optics of Rough Surfaces, Discontinuous Films and Heterogeneous Materials. *Surf. Sci.* **1980**, *96*, 1−31.

(61) Link, S.; El-Sayed, M. A. Size and Temperature Dependence of the Plasmon Absorption of Colloidal Gold Nanoparticles. *J. Phys. Chem. B* **1999**, *103*, 4212−4217.

(62) Doremus, R. H. Optical Properties of Thin Metallic Films in Island Form. *J. Appl. Phys.* **1966**, *37*, 2775−2781.

(63) Schürmann, U.; Takele, H.; Zaporojtchenko, V.; Faupel, F. Optical and Electrical Properties of Polymer Metal Nanocomposites Prepared by Magnetron Co-Sputtering. *Thin Solid Films* **2006**, *515*, 801−804.

(64) Aspnes, D. E. Optical Properties of Thin Films. *Thin Solid Films* **1982**, *89*, 249−262.

(65) Gompf, B.; Beister, J.; Brandt, T.; Pflaum, J.; Dressel, M. Nanometer-Thick Au-Films as Antireflection Coating for Infrared Light. *Opt. Lett.* **2007**, *32*, 1578−1580.

(66) Gao, W.; Kahn, A. Electrical Doping: The Impact on Interfaces of π-Conjugated Molecular Films. *J. Phys.: Condens. Matter* **2003**, *15*, S2757−S2770.

(67) Buffet, A.; Rothkirch, A.; Döhrmann, R.; Körstgens, V.; Abul Kashem, M. M.; Perlich, J.; Herzog, G.; Schwartzkopf, M.; Gehrke, R.; Müller-Buschbaum, P.; et al. P03, the Microfocus and Nanofocus X-Ray Scattering (MiNaXS) Beamline of the PETRA III Storage Ring: The Microfocus Endstation. *J. Synchrotron Radiat.* **2012**, *19*, 647−653.

(68) Santoro, G.; Buffet, A.; Döhrmann, R.; Yu, S.; Körstgens, V.; Müller-Buschbaum, P.; Gedde, U.; Hedenqvist, M.; Roth, S. V. Use of Intermediate Focus for Grazing Incidence Small and Wide Angle X-Ray Scattering Experiments at the Beamline P03 of PETRA III, DESY. *Rev. Sci. Instrum.* **2014**, *85*, 043901.

(69) Benecke, G.; Wagermaier, W.; Li, C.; Schwartzkopf, M.; Flucke, G.; Hoerth, R.; Zizak, I.; Burghammer, M.; Metwalli, E.; Müller-Buschbaum, P.; et al. A Customizable Software for Fast Reduction and Analysis of Large X-Ray Scattering Data Sets: Applications of the New DPDAK Package to Small-Angle X-Ray Scattering and Grazing-Incidence Small-Angle X-Ray Scattering. *J. Appl. Crystallogr.* **2014**, *47*, 1797−1803.